



# Ordered mesoporous Nb–W oxides for the conversion of glucose to fructose, mannose and 5-hydroxymethylfurfural

Jing Guo <sup>a,b</sup>, Shanhui Zhu <sup>a,\*</sup>, Youliang Cen <sup>a,b</sup>, Zhangfeng Qin <sup>a</sup>, Jianguo Wang <sup>a</sup>, Weibin Fan <sup>a,\*</sup>

<sup>a</sup> State Key Laboratory of Coal Conversion, Institute of Coal Chemistry, Chinese Academy of Sciences, Taiyuan 030001, PR China

<sup>b</sup> University of Chinese Academy of Sciences, Beijing 100049, PR China



## ARTICLE INFO

### Article history:

Received 7 May 2016

Received in revised form 10 July 2016

Accepted 29 July 2016

Available online 30 July 2016

### Keywords:

Glucose

Fructose

5-Hydroxymethylfurfural

Mesoporous Nb–W

Isomerization

## ABSTRACT

A series of ordered mesoporous  $\text{Nb}_x\text{W}_{(8-x)}$  oxides with tunable Nb/W ratio were successfully synthesized by evaporation-induced self-assembly method. The mesoporous structure, morphologies, surface chemical state, and acidic properties of these catalysts were fully characterized by low-temperature sorption of  $\text{N}_2$ , small-angle and wide-angle XRD, TEM, Raman, XPS, and Py-IR. It was shown that the  $\text{Nb}_x\text{W}_{(8-x)}$  oxides created large amounts of Lewis as well as Brønsted acid sites, which promoted the isomerization of glucose to fructose followed its dehydration to 5-hydroxymethylfurfural (HMF). Mannose was also formed via the epimerization of glucose. Of them, the mesoporous  $\text{Nb}_4\text{W}_4$  exhibited the best catalytic activity with a comparatively low  $E_a$  about 90.2 kJ/mol and good stability in aqueous medium. The kinetic behavior revealed that Lewis acid sites facilitated to glucose-to-fructose isomerization while Brønsted acid sites promoted the dehydration of fructose to form HMF.

© 2016 Elsevier B.V. All rights reserved.

## 1. Introduction

Biomass is considered as a promising renewable resource to cover the shortage of fossil resources and remit the serious environmental problems [1–4]. Many approaches have been proposed to obtain high-value added chemicals from biomass carbohydrates [5–7]. Glucose is the monomer of cellulose and the most available and low-cost six-carbon monosaccharide, which can also be obtained from starch and original raw material [8]. Additionally, glucose possesses five hydroxyl groups and one aldehyde group, and thus has the properties of both polyhydric alcohols and aldehyde. The abundant reserves and rich functional groups of glucose make it an ideal feedstock to synthesize various chemicals and fuels.

The isomerization of glucose to fructose is a crucial step in the process of cellulosic biorefineries [9]. Biological enzymes are employed in current industrial process [10]. However, their uses suffer from bad recovery, expensive cost and strict operating conditions. Recently, significant efforts have been made to explore robust inorganic catalysts which are able to catalyze the isomerization reaction at high temperature and highly acidic environment [11,12]. The used homogeneous chemical catalysts mainly include

inorganic alkali, inorganic acid, and metal salts such as  $\text{ZnCl}_2$ ,  $\text{AlCl}_3$ ,  $\text{CrCl}_3$  and  $\text{CrCl}_3 \cdot 6\text{H}_2\text{O}$  [13–18]. However, these homogeneous catalysts are difficult to recycle. Thus, potential heterogeneous catalysts such as solid bases and solid Lewis acids seem to be the most promising ones for isomerization. Mg-Al hydrotalcite is the typical solid base catalyst [2,19–21] and the 30% yield of fructose is obtained over hydrotalcite synthesized by co-precipitation method [2]. Molecular sieve-based catalysts, such as Si-MCM, H-USY, zeolite Y, Ti-Beta, Sn-Al-Beta, Sn-Beta, are active solid Lewis acids [9,10,12,22–31]. Moliner et al. [12] achieved high fructose yield of 31% within 30 min at 110 °C over Sn-doped Beta zeolite for the first time. Liu et al. [26] synthesized Sn-beta zeolites by a post-synthesis method, which shortened the preparation time from the previously reported 40 d to less than 1 d. Additionally, Dijkmans et al. [24] reported nearly the same productivities as the original  $\text{Sn}\beta$  with a lower Sn loading by Sn in dealuminated  $\beta$  zeolites. Mesoporous Sn-MFI zeolite and self-pillared, single-unit-cell Sn-MFI zeolite nanosheets were also explored for glucose isomerization reaction, and the latter was more active with 65% fructose yield at about 85% glucose conversion in ethanol solvent [32,33].

The formed fructose in glucose isomerization can proceed to consecutive dehydration into 5-hydroxymethylfurfural (HMF), which is an important platform molecule [9,34,35]. Apart from fructose and HMF, mannose is also usually generated as a major byproduct in glucose conversion [10,36–38]. It is generally

\* Corresponding authors.

E-mail addresses: [zhushanhui@sxicc.ac.cn](mailto:zhushanhui@sxicc.ac.cn) (S. Zhu), [fanwb@sxicc.ac.cn](mailto:fanwb@sxicc.ac.cn) (W. Fan).

accepted that the glucose-fructose isomerization and glucose-mannose epimerization are catalyzed by Lewis acid, while the dehydration reaction of fructose is typically activated by Brønsted acid [39]. However, recent kinetic experimental shows that glucose-fructose conversion is catalyzed not only by the Lewis acidity of metal cations, but also by the Brønsted acidity of the water complexes of the cations [29]. Choudhary et al. [39] found the interplay of Brønsted acid and Lewis acid in glucose conversion to HMF over  $\text{CrCl}_3$  combined with HCl. Wrigstedt et al. [40] reported the role of Brønsted acid in the reaction of aqueous-phase glucose dehydration to HMF which was catalyzed by Lewis acids. Nevertheless, there's no study about the influence of Brønsted acid and Lewis acid of heterogeneous catalyst to the glucose conversion.

The use of mesoporous transition-metal oxide materials is a promising approach to develop heterogeneous catalysts with enhanced activity because of the effective exposure of active sites to reactants and acceleration of the diffusion rate of molecules [41,42]. Tagusagawa et al. [43,44] successfully synthesized mesoporous  $\text{Nb}_2\text{O}_5$ – $\text{WO}_3$  and  $\text{Ta}_2\text{O}_5$ – $\text{WO}_3$  catalysts, and these materials exhibited remarkable performance for the liquid-phase Friedel–Crafts alkylation owing to their high surface area, mesoporous structure, and strong Brønsted acid sites. Although mesoporous oxides display outstanding catalytic performance in various acid-catalyzed reactions, their applications in aqueous-phase biomass conversion have rarely been reported because the solvent water usually deteriorates the mesoporous structure and seriously affects the reactivity.

It's well-known that glucose is strongly hydrophilic and the glucose from the hydrolysis of cellulose or polysaccharide contains water unavoidably, which makes water the most desired solvent for glucose conversion in view of environmental and economical viability. Herein, for the first time, a series of robust mesoporous Nb–W oxides catalysts with tunable compositions were explored in glucose conversion reaction using green media water. These catalysts were fully characterized by various techniques including low-temperature sorption of  $\text{N}_2$ , small-angle and wide-angle XRD, TEM, Raman, XPS and FTIR of adsorbed pyridine. The catalyst structure, structure-activity relationship and kinetic behavior were discussed in detail. Special attention will paid to the role of Brønsted acid and Lewis acid in glucose conversion.

## 2. Experimental

### 2.1. Catalyst preparation

Mesoporous Nb–W mixed oxides were synthesized according to previously reported evaporation-induced self-assembly method [43]. 6 mmol mixed  $\text{NbCl}_5$  (Aladdin) and  $\text{WCl}_6$  (Aladdin) were added to a solution of Pluronic P-123 (Aldrich, 1 g) which was used as a structure-directing agent in *n*-propanol (10 g) under vigorous stirring. After the complete dissolution of metal chlorides, 30 mmol water was added dropwise and the mixture was further stirred at room temperature for 2 h. The resulting sol solution was gelled in a PTFE beaker (100 mL) at 40 °C for 10–20 days. The aged gel samples were finally calcined at 450 °C for 10 h in flowing air. The as-prepared catalysts were designated as  $\text{Nb}_x\text{W}_{(8-x)}$  ( $x = 1, 3, 4, 5$  and 7), where  $x$  denotes the molar fraction of Nb with W.

### 2.2. Catalyst characterization

$\text{N}_2$  adsorption/desorption isotherms were measured at –196 °C on a BELSORP-max gas adsorption analyzer after the samples were degassed at 300 °C to remove physically adsorbed impurities under high vacuum for 8 h. The specific surface area was calculated by

Brunauer–Emmett–Teller (BET) method and the pore size distribution was derived from Barrett–Joyner–Halenda (BJH) method.

Wide-angle X-ray powder diffraction (XRD) patterns were collected on a Rigaku MiniFlex II desktop X-ray diffractometer with monochromated  $\text{Cu K}\alpha$  radiation at 30 kV and 15 mA at a scanning speed ( $2\theta$ ) of 2°/min. For small-angle X-ray diffraction (XRD) measurements, the XRD patterns were obtained on a Bruker D8 ADVANCE X-ray diffractometer with  $\text{Cu K}\alpha$  radiation at 40 kV and 40 mA. All XRD patterns were collected in the  $2\theta$  range of 0.5–10° at a scanning rate of 1°/min.

Transmission electron microscope (TEM) was taken on a field emission transmission electron microscope (JEM-2100F) at an acceleration voltage of 200 kV. Prior to the tests, the sample powders were dispersed in ethanol with ultrasonication for 15 min and dropped onto copper grids.

X-ray photoelectron spectroscopy (XPS) were performed on a Kratos AXIS ULTRA DLD spectrometer with a monochromated  $\text{Al K}\alpha$  radiation source ( $h\nu = 1486.6$  eV) and a multichannel detector. All spectra were recorded by using an aperture slot of  $300 \times 700 \mu\text{m}$ , and survey spectra were recorded with a pass energy of 160 eV while high-resolution spectra with a pass energy of 40 eV. The binding energies were calibrated by the adventitious C 1s peak at 284.8 eV as reference. The experiment error was given within  $\pm 0.1$  eV.

Raman spectroscopy was measured at room temperature on a LabRAM HR800 System equipped with a CCD detector. The He–Cd laser (325 nm) was used as the exciting source with a power of 30 MW.

The pyridine adsorption FTIR spectra (Py-IR) were conducted on a Bruker TENSOR 27 spectrometer to probe the accessible surface acid sites. The powder samples were pressed into translucent disks, degassed in vacuum at 400 °C for 2 h, exposed to pyridine vapor, and then cooled down to 35 °C. The Py-IR spectra were then recorded at 150 °C after applying vacuum for 30 min. The concentration of acidic sites was calculated by the procedures reported by Madeira et al. [45].

### 2.3. Catalytic reaction

All the catalytic reactions were carried out in a Teflon-lined autoclave (30 mL) with magnetic stirring apparatus. Typically, 10 g 4.5 wt.% aqueous solution of reactant and 0.2 g catalyst were introduced into the reactor. When the temperature reached 120 °C, the stirring button was opened and the reaction started. After the reaction, the reactor was quickly cooled in an ice-water bath.

The solid catalyst and the reaction mixture were separated by centrifugation, and then a small amount of clear filtrate was removed for analysis. The reactant and products were determined by a high performance liquid chromatograph (HPLC, Waters 2695) equipped with a XBRIDGE Amide column (3.5  $\mu\text{m}$  4.6 mm  $\times$  150 mm) and a refractive index detector (Waters 2414). The analysis conditions were listed below: mobile phase acetonitrile/water/ammonium hydroxide (80:20:0.1 in volume ratio), flow rate 0.4 mL/min, column temperature 35 °C, and detector temperature 40 °C. The content of HMF, fructose, mannose, and glucose in the samples was obtained using external standard method. The reactant conversion and product yield were calculated as follows:

$$\text{Conversion}(\%) = \frac{\text{mol of reactant initial} - \text{mol of reactant final}}{\text{mol of reactant initial}} \times 100$$

$$\text{Yield}(\%) = \frac{\text{mol of product produced}}{\text{mol of reactant initial}} \times 100$$

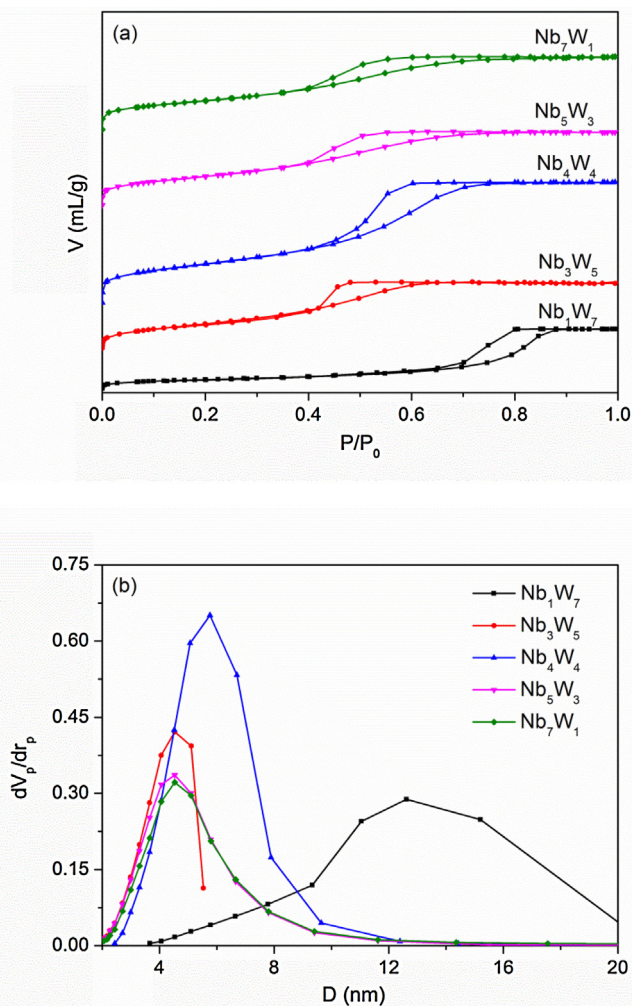


**Fig. 1.** (a)  $N_2$  adsorption-desorption isotherms and (b) pore size distributions curves of  $Nb_xW_{(8-x)}$  oxides.

### 3. Results and discussion

#### 3.1. Characterization of the catalysts

##### 3.1.1. Physicochemical properties and morphology

The  $N_2$  adsorption/desorption isotherms and pore diameter distributions of mesoporous  $Nb_xW_{(8-x)}$  oxide catalysts are compiled in Fig. 1. As shown in Fig. 1a, all of the samples showed type IV isotherm with H1 hysteresis loop at the high relative pressure region. According to Fig. 1b, this nitrogen uptake step for  $Nb_xW_{(8-x)}$  displayed relatively narrow pore size distribution, which revealed the presence of uniform mesopores except for  $Nb_1W_7$  with wide pore diameter distribution. Additionally, it can be seen that the mesoporous structure orderliness in  $Nb_4W_4$  are better than other samples. As displayed in Table 1, the surface area of  $Nb_xW_{(8-x)}$  increased gradually with the increasing tungsten content, maximized at  $Nb_4W_4$  ( $123\text{ m}^2/\text{g}$ ), and then declined.

Fig. 2 illustrates the small-angle X-ray diffraction (XRD) patterns for the catalyst samples. The  $Nb_xW_{(8-x)}$  ( $x = 3-7$ ) samples showed remarkable diffraction peaks at  $2\theta$  range of  $0.5-1.5^\circ$ , suggesting that these samples possessed well-ordered mesoporous structure. However, no diffraction peak was detected in  $Nb_1W_7$ , reflecting its bad mesoporous structure, consistent well with the  $N_2$  adsorption/desorption result.

The TEM images of  $Nb_xW_{(8-x)}$  catalysts are shown in Fig. 3. Consistent with the small-angle XRD results, the wormhole-like

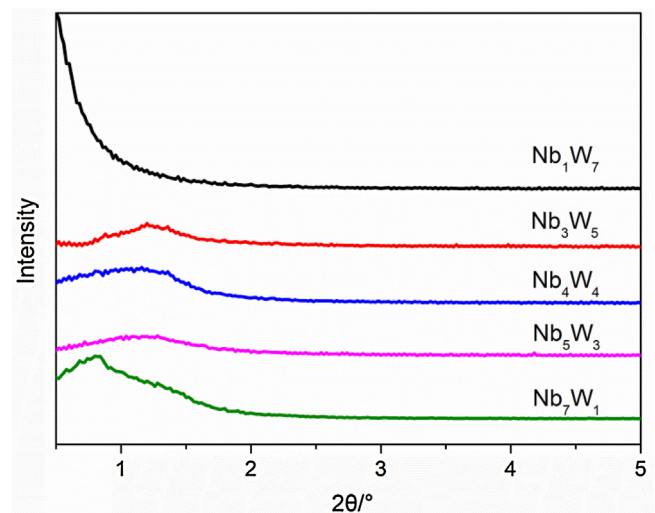


**Fig. 2.** Small-angle powder XRD patterns of  $Nb_xW_{(8-x)}$  oxides.

**Table 1**  
Surface area and the concentration of acid sites of  $Nb_xW_{(8-x)}$  oxides.

| Catalyst  | $S_{\text{BET}}$ ( $\text{m}^2\text{g}^{-1}$ ) | $C_B$ ( $\text{umol g}^{-1}$ ) | $C_L$ ( $\text{umol g}^{-1}$ ) | $C_B/C_L$ |
|-----------|--|--------------------------------|--------------------------------|-----------|
| $Nb_1W_7$ | 35.2   | 19.4                           | 41.2                           | 0.47      |
| $Nb_3W_5$ | 98.6   | 73.0                           | 98.1                           | 0.74      |
| $Nb_4W_4$ | 123.2  | 69.2                           | 99.0                           | 0.70      |
| $Nb_5W_3$ | 96.6   | 67.1                           | 102.4                          | 0.66      |
| $Nb_7W_1$ | 89.2   | 34.9                           | 95.1                           | 0.37      |

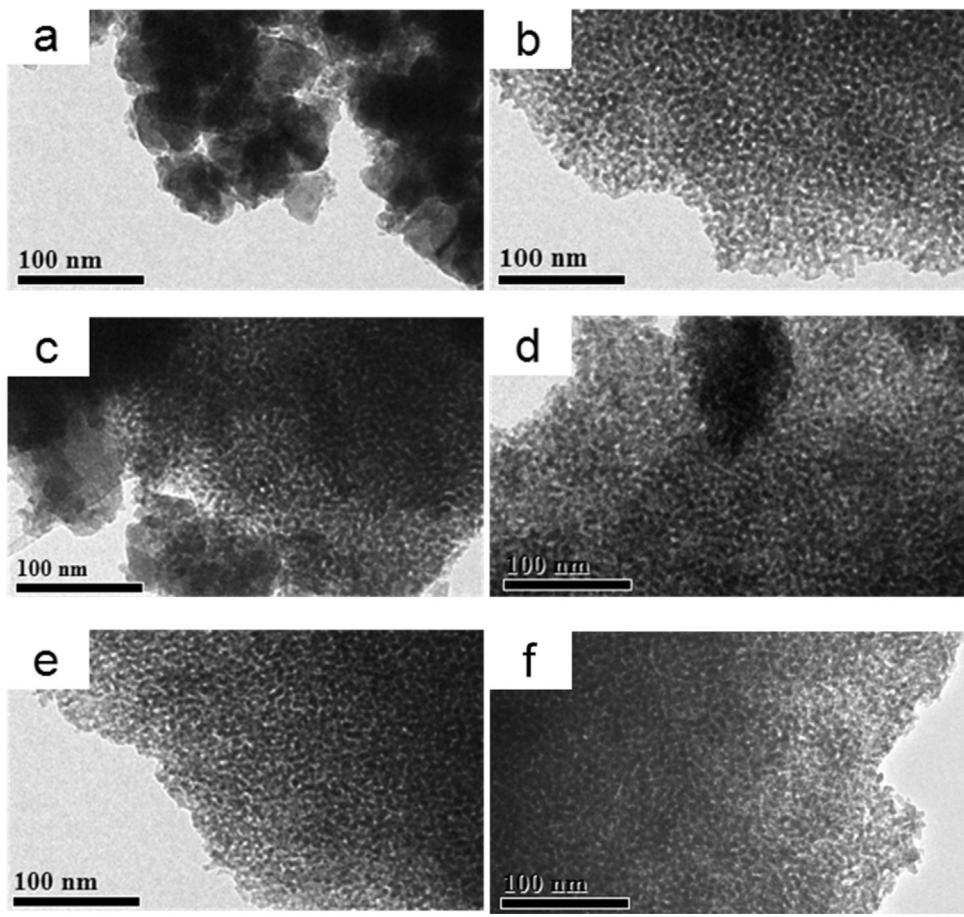
ordered mesopores were clearly observed in the  $Nb_xW_{(8-x)}$  mixed oxides (Fig. 3(b–e)). However, there were only bulk-like particles with accumulation void in the image of  $Nb_1W_7$ . Thus, the presence of hysteresis loop in the  $N_2$  adsorption/desorption isotherm of  $Nb_1W_7$  may be due to the space that was formed from particle accumulation.

Based on the  $N_2$  adsorption/desorption analysis, small-angle XRD and TEM results, the ordered mesoporous  $Nb_7W_1$ ,  $Nb_5W_3$ ,  $Nb_4W_4$  and  $Nb_3W_5$  are successfully synthesized. However, there is no mesopore in  $Nb_1W_7$  oxide. The high tungsten content is adverse to the formation of mesopore structure, as reported in previous literature [43].

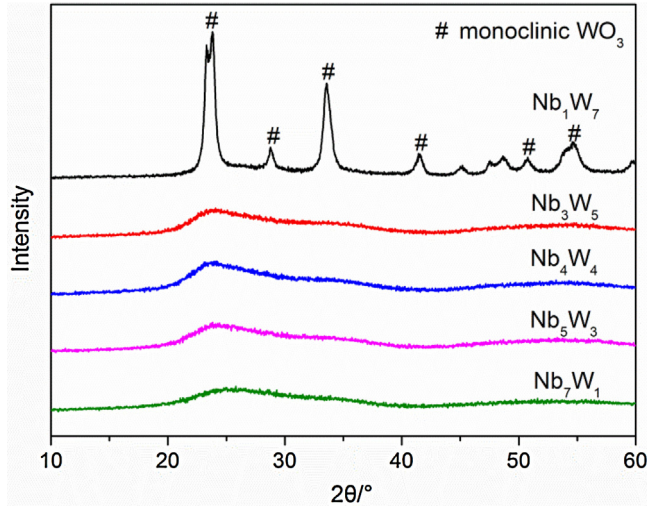
##### 3.1.2. Catalyst structure and chemical state

Fig. 4 shows the wide-angle X-ray diffraction (XRD) patterns of  $Nb$ -W oxides. The intensities and shapes of diffraction peaks in ordered mesoporous  $Nb_xW_{(8-x)}$  ( $x = 3-7$ ) were quite similar and only broad and diffuse diffractions were detected. No diffraction peaks corresponding to niobium and tungsten species were observed, which should be due to the high dispersion of niobium and tungsten species or their amorphous state. However, in the XRD pattern of  $Nb_1W_7$  the sharp peaks at  $2\theta = 23^\circ, 28^\circ, 34^\circ, 42^\circ, 50^\circ$  and  $55^\circ$  were related to monoclinic  $WO_3$  [46]. Thus,  $WO_3$  changed from highly dispersed form to crystalline state with the increase of tungsten content.

Raman spectra are further employed to identify the surface geometric structure of the samples. As illustrated in Fig. 5, the characteristic bands of  $Nb_2O_5$  did not appear. The absence of Raman-active modes corresponding to niobium oxides reveals that  $Nb_2O_5$  is amorphous in  $Nb_xW_{(8-x)}$ . The typical Raman bands for m- $WO_3$  phase centered at  $274, 715$  and  $808\text{ cm}^{-1}$  were only obvious in  $Nb_1W_7$  oxide [47], in well line with the XRD results. Moreover, the intensity of these bands decreased with the increase of  $Nb_2O_5$  content, reflecting that the incorporation of  $Nb_2O_5$  improved the dispersion of  $WO_3$  species, most probably due to the enhanced



**Fig. 3.** TEM images of (a) non-mesoporous  $\text{Nb}_1\text{W}_7$ , mesoporous (b)  $\text{Nb}_3\text{W}_5$ , (c)  $\text{Nb}_4\text{W}_4$ , (d)  $\text{Nb}_5\text{W}_3$ , (e)  $\text{Nb}_7\text{W}_1$  and (f) mesoporous  $\text{Nb}_4\text{W}_4$  after four reuse cycles.



**Fig. 4.** Wide-angle powder XRD patterns of  $\text{Nb}_x\text{W}_{(8-x)}$  oxides.

interaction. Another band centered at  $973\text{ cm}^{-1}$  was associated with the stretch mode of monooxo  $\text{W}=\text{O}$  species corresponding to highly dispersed  $\text{WO}_x$  species [48]. Meanwhile, this band shifted gradually from  $973\text{ cm}^{-1}$  to  $932\text{ cm}^{-1}$  with the increasing  $\text{Nb}_2\text{O}_5$  content, revealing that the bulk  $\text{WO}_3$  crystallites gradually transformed into polytungstate species and even isolated mono-tungstate species [47].

The existence states of niobium and tungsten species in  $\text{Nb}_x\text{W}_{(8-x)}$  catalysts were investigated by XPS technique. The Nb,

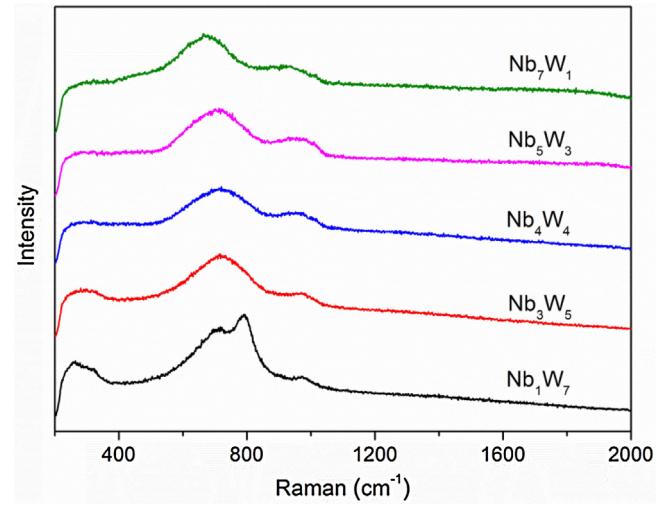


**Fig. 5.** Raman spectra of  $\text{Nb}_x\text{W}_{(8-x)}$  oxides.

O and W were detected as exclusive elements in  $\text{Nb}_x\text{W}_{(8-x)}$ , ruling out the possible influences from impurities. As shown in Fig. 6a, the two peaks at 209.9 and 207.1 eV were ascribed to  $3\text{d}_{3/2}$  and  $3\text{d}_{5/2}$  of  $\text{Nb}_2\text{O}_5$  [49], respectively. As illustrated in Fig. 6b, the peaks at 37.9 and 35.7 eV were corresponding to  $4\text{f}_{1/2}$  and  $4\text{f}_{3/2}$  of  $\text{WO}_3$  [50]. Both the binding energy of Nb 3d and W 4f moved to the direction of higher binding energy with the increasing Nb content, indicating the change of electron density in the W and Nb nucleus. This is

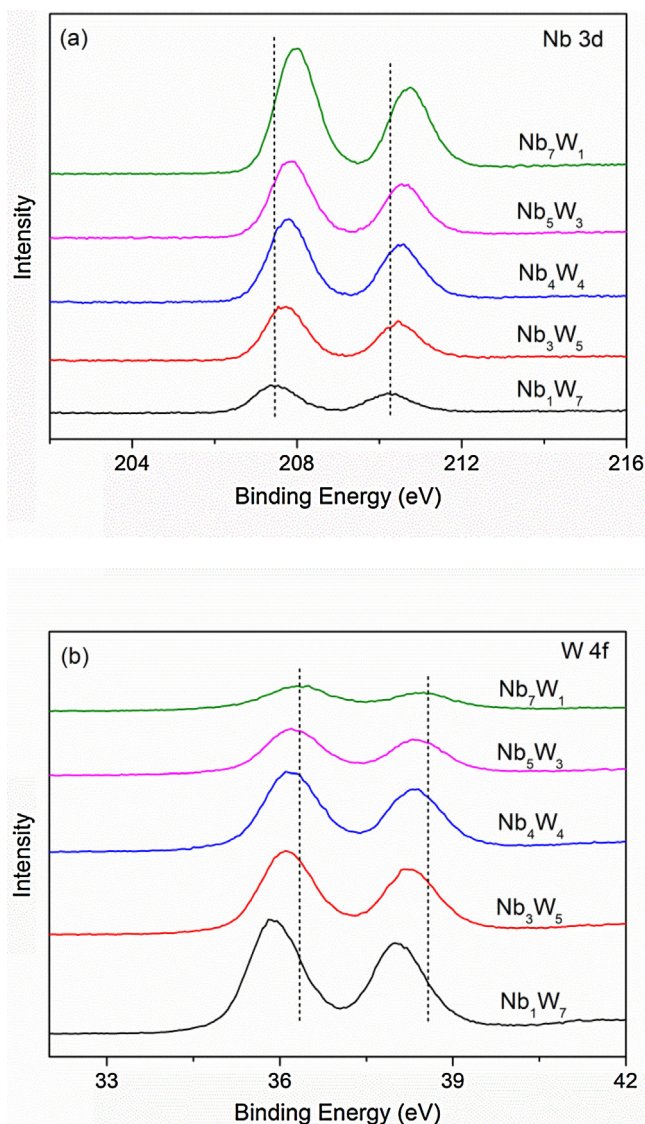


Fig. 6. (a) Nb 3d and (b) W 4f XPS of  $\text{Nb}_x\text{W}_{(8-x)}$  ( $x = 1, 3, 4, 5, 7$ ) oxides.

caused by the different chemical states of  $\text{WO}_3$  and  $\text{Nb}_2\text{O}_5$  in these  $\text{Nb}_x\text{W}_{(8-x)}$  catalysts with different ratio of Nb and W.

As indicated by XRD, Raman and XPS, the molecular structure of  $\text{WO}_x$  over  $\text{Nb}_x\text{W}_{(8-x)}$  catalysts exists in the form of monotungstate, polytungstate and crystalline m- $\text{WO}_3$  clusters, which strongly depends on  $\text{WO}_3$  content.  $\text{Nb}_7\text{W}_1$  should be predominantly consisted of isolated monotungstate species in highly dispersed states because of rather low  $\text{WO}_3$  content. With increasing  $\text{WO}_3$  content, the monotungstate species gradually transforms into polytungstate. The XRD result reflects that  $\text{Nb}_1\text{W}_7$  primarily contains crystalline m- $\text{WO}_3$ .

### 3.1.3. Acidity properties

The FTIR profiles for adsorbed pyridine by  $\text{Nb}_x\text{W}_{(8-x)}$  catalysts are displayed in Fig. 7. The band at  $\sim 1540 \text{ cm}^{-1}$  was assigned to Brønsted acidic sites. The peak at  $1440 \text{ cm}^{-1}$  was obvious, which was attributed to coordinatively bound pyridine on Lewis acidic sites. The  $\text{Nb}_x\text{W}_{(8-x)}$  surface is covered by both Brønsted acidic sites and Lewis acidic sites, because isomorphous replacement of  $\text{Nb}^{5+}$  with higher-valence  $\text{W}^{6+}$  cations forms strong Brønsted acid sites [51]. The Brønsted acidic sites of  $\text{Nb}_x\text{W}_{(8-x)}$  (except  $\text{Nb}_1\text{W}_7$ ) increased with increasing tungsten content due to the for-

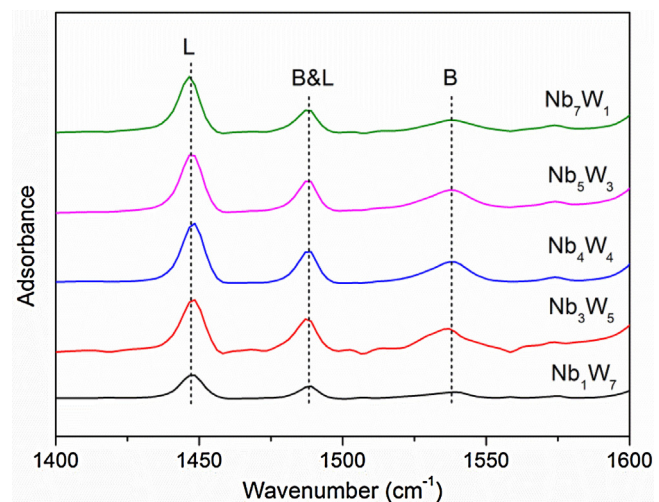


Fig. 7. FT-IR spectra for pyridine adsorbed by  $\text{Nb}_x\text{W}_{(8-x)}$  ( $x = 1, 3, 4, 5, 7$ ) oxides.

Table 2

The glucose conversion and yields of fructose, mannose, and HMF after reaction for 120 min.

| Catalyst                | Conversion (%) | Yield (%) |         |      |
|-------------------------|----------------|-----------|---------|------|
|                         |                | Fructose  | Mannose | HMF  |
| $\text{Nb}_1\text{W}_7$ | 11.6           | 2.3       | 5.5     | 3.3  |
| $\text{Nb}_3\text{W}_5$ | 32.2           | 2.4       | 9.3     | 10.3 |
| $\text{Nb}_4\text{W}_4$ | 36.1           | 2.3       | 5.3     | 18.8 |
| $\text{Nb}_5\text{W}_3$ | 29.1           | 3.0       | 4.5     | 10.7 |
| $\text{Nb}_7\text{W}_1$ | 30.4           | 2.9       | 2.8     | 12.4 |

mation of polytungstate species [44]. According to earlier study on  $\text{WO}_x/\text{Al}_2\text{O}_3$  and  $\text{WO}_3/\text{ZrO}_2$  systems [47,52], the surface monotungstate species at low  $\text{WO}_x$  content display small acidity, while polytungstate species possess strong acidity owing to the generation of interconnected  $\text{WO}_x$  species. Contrarily, Brønsted acidic sites in  $\text{Nb}_1\text{W}_7$  decreased sharply because of the formation of crystalline  $\text{WO}_3$ , which did not contribute to the Brønsted acidic sites. Additionally, the low content of Nb in  $\text{Nb}_1\text{W}_7$  may also affect the total acidity, because  $\text{Nb}_2\text{O}_5$  possesses some intrinsically acidic sites. Besides the concrete data of Brønsted acid sites concentration, the concentration of Lewis acidic sites and ratio of Brønsted acid sites and Lewis acidic sites are also displayed in Table 1.

### 3.2. Catalytic performance of the catalysts

#### 3.2.1. Effect of the molar ratio of Nb and W on the catalytic performance of glucose conversion

All the reactions were conducted in the range of low conversion to explore the intrinsically kinetic behavior. The time evolution of glucose conversion and fructose, mannose and HMF yields over  $\text{Nb}_x\text{W}_{(8-x)}$  at  $120^\circ\text{C}$  is displayed in Fig. 8. The reaction results for 120 min are listed in Table 2. Glucose conversion decreased as 36%, 32%, 30%, 29% and 11% when employing  $\text{Nb}_4\text{W}_4$ ,  $\text{Nb}_3\text{W}_5$ ,  $\text{Nb}_7\text{W}_1$ ,  $\text{Nb}_5\text{W}_3$ , and  $\text{Nb}_1\text{W}_7$  as catalysts after reaction for 2 h in aqueous medium, respectively. This result is in good agreement with surface area that the glucose conversion increases with the increase of surface area. The ordered mesoporous network improves the accessible surface area, and contributes to a better diffusion of reactants and products. Therefore, the tailored mesoporous structure appears to be a key to determine the catalytic behavior. Besides the mesoporous structure, surface acidic site is also an important factor to the catalytic activity. Generally, the formation of fructose from glucose is catalyzed by Lewis acid via a 1,2 intramolecular hydride

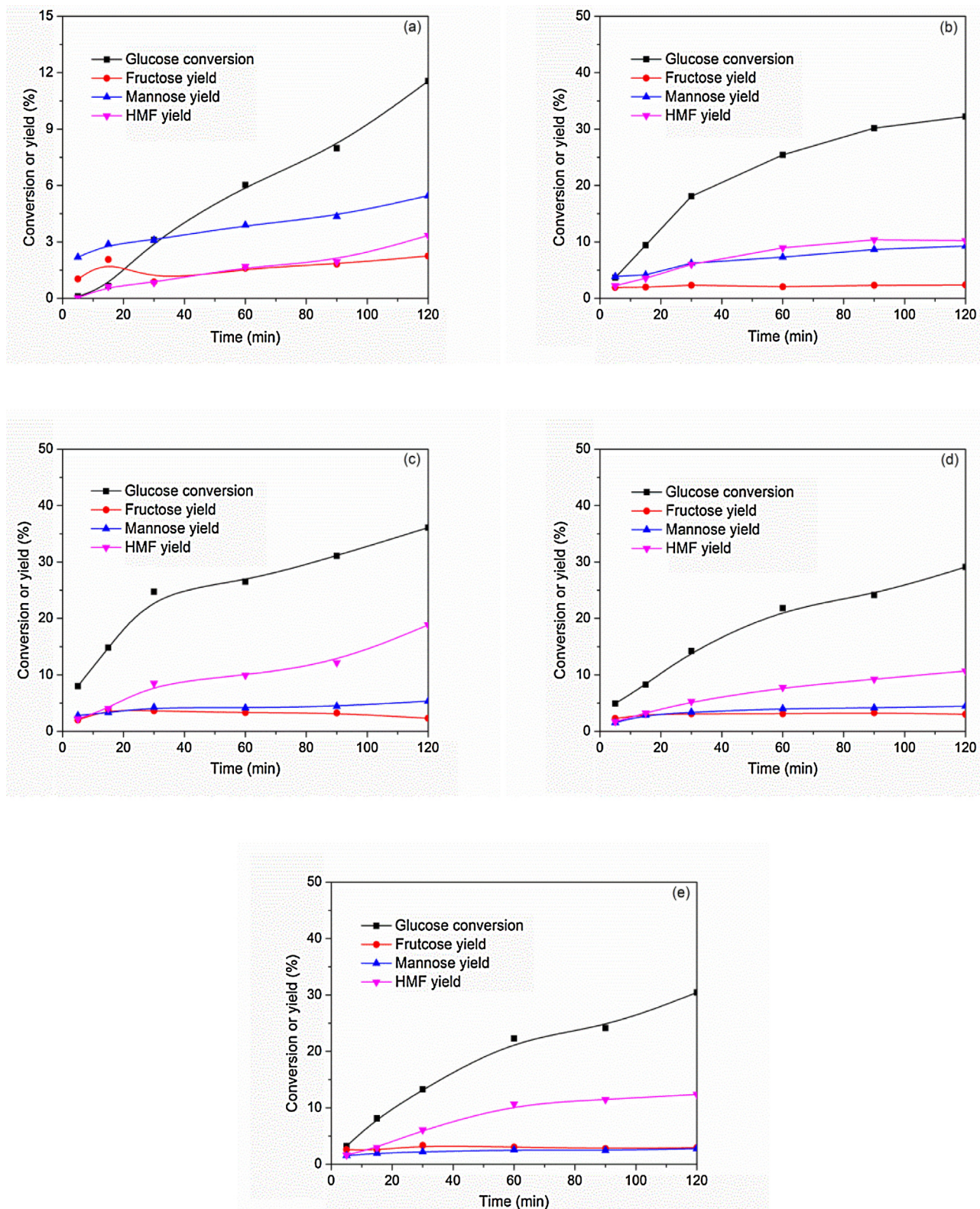


**Fig. 8.** Glucose conversion using (a) Nb<sub>1</sub>W<sub>7</sub>, (b) Nb<sub>3</sub>W<sub>5</sub>, (c) Nb<sub>4</sub>W<sub>4</sub>, (d) Nb<sub>5</sub>W<sub>3</sub> and (e) Nb<sub>7</sub>W<sub>1</sub> as catalysts in aqueous medium.

transfer, while HMF comes from the consecutive dehydration of fructose over Brønsted acid. Lewis acid is also the active site for the epimerization of glucose to mannose by either two subsequent intramolecular hydride transfer steps or one 1,2 intramolecular carbon shift step [53,54]. Of them, Nb<sub>4</sub>W<sub>4</sub> gave the maximum conversion of glucose, as it possessed large amounts of acidity and the

highest ordered mesoporous structure. As revealed by XRD, Raman and XPS, the WO<sub>3</sub> species exist mainly as highly dispersed polytungstate states in Nb<sub>4</sub>W<sub>4</sub> surface. Moreover, the polytungstate species contributes to the most acid sites. Accordingly, it is reasonably inferred that the polytungstate states are the dominant active sites for glucose conversion. Additionally, Nb<sub>1</sub>W<sub>7</sub> gave the low-

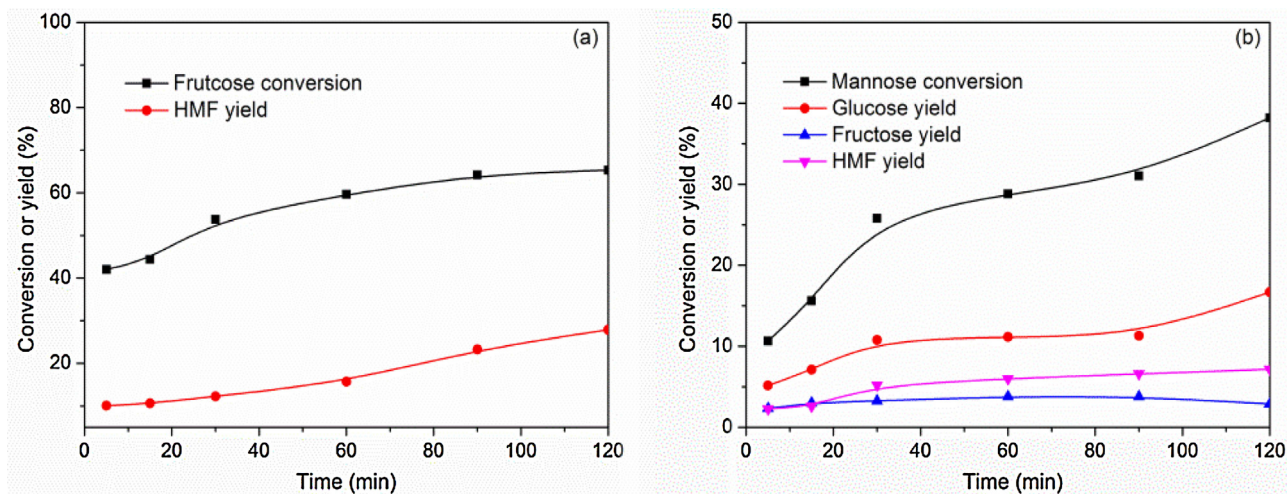


Fig. 9. (a) Fructose conversion and (b) mannose conversion over  $\text{Nb}_4\text{W}_4$  in aqueous medium.

est glucose activity, because it predominantly contains weak acidic crystalline  $\text{m-WO}_3$  and shows non-mesoporous structure.

As illustrated in Fig. 8, the yield of fructose was low and kept stable with increasing reaction time, because the glucose-fructose isomerization is an equilibrium-limited reaction and the formed fructose easily proceeds further dehydration to HMF. This indicates that glucose-fructose isomerization may be the rate-determining step of glucose-HMF conversion. Based on Tables 1 and 2, it can be seen that the yield of fructose declines with the increasing concentration of Brønsted acid sites because the presence of Brønsted acid is adverse to the glucose-fructose isomerization, and promotes its conversion to HMF [39]. The yield of HMF increased obviously with the increasing time, because the Brønsted acid facilitated to catalyze ketose-dehydration reaction and further drove the aldehyde-ketose conversion step. As shown in Tables 1 and 2, the yield of HMF increases with the increasing concentration of Brønsted acid sites, confirming that the Brønsted acid is actually the efficient active site for fructose dehydration reaction. Of them, the highest HMF yield of 18.8% was obtained over  $\text{Nb}_4\text{W}_4$ . The yield of mannose increased with time but very slowly, suggesting that it gradually approached aldose-ketose equilibrium. The yield of mannose decreased with the decrease of W content (except  $\text{Nb}_1\text{W}_7$ ), indicating that the presence of Brønsted acid was probably favorable for the formation of mannose. This result is inconsistent with the previously published data [53]. According to Fig. 9a, no mannose is produced from fructose at all. Therefore, we conclude that the epimerization of glucose to mannose proceeds by one 1,2 intramolecular carbon shift step over  $\text{Nb}_x\text{W}_{(8-x)}$  oxides. The earlier report has demonstrated that the epimerization reaction is very sensitive to the pH of the molybdcic acid solution with  $\text{Mo}^{\text{VI}}$  dimer activity center [55]. In addition, Chethana et al. [56] indicates that pH plays important role in the 1,2 carbon shift reaction in sugar molecules by changing the structural flexibility of the metal complex and the concentration of the dimeric  $\text{Mo}^{\text{VI}}$  species is maximal under optimized conditions (pH 1.5–3.5). Unlike Sn-Beta, Brønsted acid sites and Lewis acidic sites exist in solid  $\text{Nb}_x\text{W}_{(8-x)}$  simultaneously in considerable amount. The presence of Brønsted acid sites decreases the pH value of the environment around Lewis acid active center. Therefore, Brønsted acid can promote the formation of mannose in part, while the Lewis acid should play a predominant role over  $\text{Nb}_x\text{W}_{(8-x)}$ .

It can be observed that the distribution of products can be regulated by using different catalysts with the tunable Brønsted acid and Lewis acid content. At the beginning of reaction, the product yields from high to low are in the sequence of mannose, HMF and fruc-

Table 3  
Reaction rate constants of glucose, fructose, mannose catalyzed by  $\text{Nb}_4\text{W}_4$ .

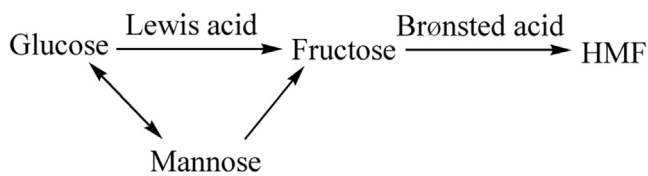
| Reactant | Catalyst                | $k (\text{s}^{-1})$   | Corresponding concentration profile |
|----------|-------------------------|-----------------------|-------------------------------------|
| glucose  | $\text{Nb}_4\text{W}_4$ | $1.34 \times 10^{-4}$ | Fig. 8c                             |
| fructose | $\text{Nb}_4\text{W}_4$ | $3.58 \times 10^{-4}$ | Fig. 9a                             |
| mannose  | $\text{Nb}_4\text{W}_4$ | $1.40 \times 10^{-4}$ | Fig. 9b                             |

tose over  $\text{Nb}_3\text{W}_5$  and  $\text{Nb}_4\text{W}_4$ . However, the order is changed into fructose, HMF and mannose over  $\text{Nb}_5\text{W}_3$  and  $\text{Nb}_7\text{W}_1$ .  $\text{Nb}_3\text{W}_5$  and  $\text{Nb}_4\text{W}_4$  possesses more Brønsted acidic sites, which are beneficial for glucose-mannose epimerization as well as dehydration reaction, and suppressing isomerization reaction. With the extended reaction time to 2 h, the order of product yield from high to low is HMF, mannose and fructose for  $\text{Nb}_3\text{W}_5$ ,  $\text{Nb}_4\text{W}_4$  and  $\text{Nb}_5\text{W}_3$ . Nevertheless, the sequence is changed into HMF, fructose, and mannose over  $\text{Nb}_7\text{W}_1$  because of its low Brønsted acidic sites.

Thus, glucose-fructose isomerization is mainly catalyzed by Lewis acidic sites and the presence of Brønsted acidic sites can suppress the yield of fructose at the beginning of the reaction. The fructose dehydration reaction is easy to carry out at the presence of Brønsted acidic sites, which can further promote the glucose-fructose isomerization. In addition, the high ratio of Brønsted acid and Lewis acid is favorable for the glucose-mannose epimerization. To obtain high HMF yield, we need chose catalyst with high amount of Brønsted acid but moderate ratio of Brønsted acid and Lewis acid, while if we want to gain mannose, we should chose catalyst with comparatively high ratio of Brønsted acid and Lewis acid. As for the formation of fructose, it behaves like a trade-off process when the Brønsted acid and Lewis acid are present at the same time.

### 3.2.2. Reaction network of glucose conversion

We also employed fructose and mannose as reactants and  $\text{Nb}_4\text{W}_4$  as catalyst to explore the network of glucose conversion. As shown in Fig. 9, fructose mainly transformed to HMF, while mannose converted to glucose, fructose and HMF. This is inconsistent with previous result that glucose, fructose and mannose can transform into each other in certain circumstances [39]. Because our  $\text{Nb}_4\text{W}_4$  catalyst possesses high ratio of Brønsted to Lewis acid sites, it promotes the dehydration to form HMF and retards the isomerization and epimerization. Compared to glucose, the reaction finished with little amount of HMF if starting from mannose (7%). According to Table 3, the reaction rate constants of fructose, mannose and glucose are estimated at  $3.58 \times 10^{-4}$ ,  $1.40 \times 10^{-4}$  and  $1.34 \times 10^{-4} \text{ s}^{-1}$ , respectively (the arithmetic is same). The conver-



**Scheme 1.** The conversion of glucose to fructose, mannose and HMF.

sion of fructose was 20% for 0 min. The reaction rate constant was calculated to adopt the results of fructose conversion for 0 min, 5 min and 15 min, while the data was chosen on substrate conversion for 5 min, 15 min and 30 min for glucose and mannose. This result verifies that the isomerization of glucose to fructose should be the rate-determining step in the conversion of glucose to HMF. Moreover, fructose favorably converts to HMF rather than glucose and mannose. The reaction pathway of glucose conversion is summarized in **Scheme 1**.

### 3.3. Kinetic analysis

The kinetics experiments of glucose conversion were carried out over  $\text{Nb}_4\text{W}_4$  at 100–120 °C under intense agitation to eliminate mass-transfer resistance. The rate constants were calculated by fitting a first-order rate expression to the glucose concentration profiles at low conversion. The reaction rate constants  $k$  calculated from the slopes of the plot in **Fig. 10a** are  $6.10 \times 10^{-6}$ ,  $1.57 \times 10^{-5}$  and  $2.67 \times 10^{-5} \text{ s}^{-1}$  at 100 °C, 110 °C and 120 °C, respectively. The Arrhenius plot based on the linear of  $k$  versus  $1/T$  is depicted in **Fig. 10b**, and the estimated apparent activation energy  $E_a$  is 90.2 kJ/mol. This value is slightly lower than that of the most active solid Lewis acid Sn-Beta (95 kJ/mol) for the isomerization of glucose [10]. The lower activation barrier clearly demonstrates the outstanding activity of  $\text{Nb}_4\text{W}_4$  for glucose conversion.

The catalytic performance of  $\text{Nb}_4\text{W}_4$  and representative catalysts for the isomerization of glucose in aqueous solution is listed in **Table 4**.  $\text{Nb}_4\text{W}_4$  gave higher glucose conversion than  $\text{AlCl}_3 \cdot 6\text{H}_2\text{O}$  in shorter time at the same temperature. The reaction rate constant of  $\text{Nb}_4\text{W}_4$  is slightly less than that of  $\text{CrCl}_3 \cdot 6\text{H}_2\text{O}$  and Sn-Beta. The advantage of  $\text{Nb}_4\text{W}_4$  is the coexistence of Lewis and Brønsted acids to achieve “one-pot” transformation of glucose to HMF. In spite of the lower fructose yield on  $\text{Nb}_4\text{W}_4$  than Sn-Beta, the yield of HMF is up to 20% without additional HCl. Moreover,  $\text{Nb}_4\text{W}_4$  is more stable than zeolites such as Sn-Beta and meso-Sn-MFI because zeolites topology structure will be confronted with severe collapse in long-term test at hot water in the presence of soluble acids [57].

### 3.4. Recycling of catalyst

A key problem for mesoporous metal oxides is the stability of the mesostructures during liquid phase reaction, particularly in aqueous solution. The reusability test for aqueous-phase conversion of glucose was conducted under the same conditions after the recovered  $\text{Nb}_4\text{W}_4$  was calcined under 400 °C for 4 h to remove residue. As displayed in **Fig. 11**,  $\text{Nb}_4\text{W}_4$  maintained its original activity and product distribution after four reaction cycles. As illustrated in **Fig. 3f**, the TEM image of spent  $\text{Nb}_4\text{W}_4$  showed that wormhole-like mesoporous structure still existed and completely preserved after four reaction cycles. The above results suggest that the mesoporous  $\text{Nb}_4\text{W}_4$  catalyst has good structure stability, even in the aqueous solution. The mesoporous  $\text{Nb}_4\text{W}_4$  oxide is a water-tolerant catalyst, and the hydrophobic open-framework structure can effectively protect Brønsted acidic sites from water.

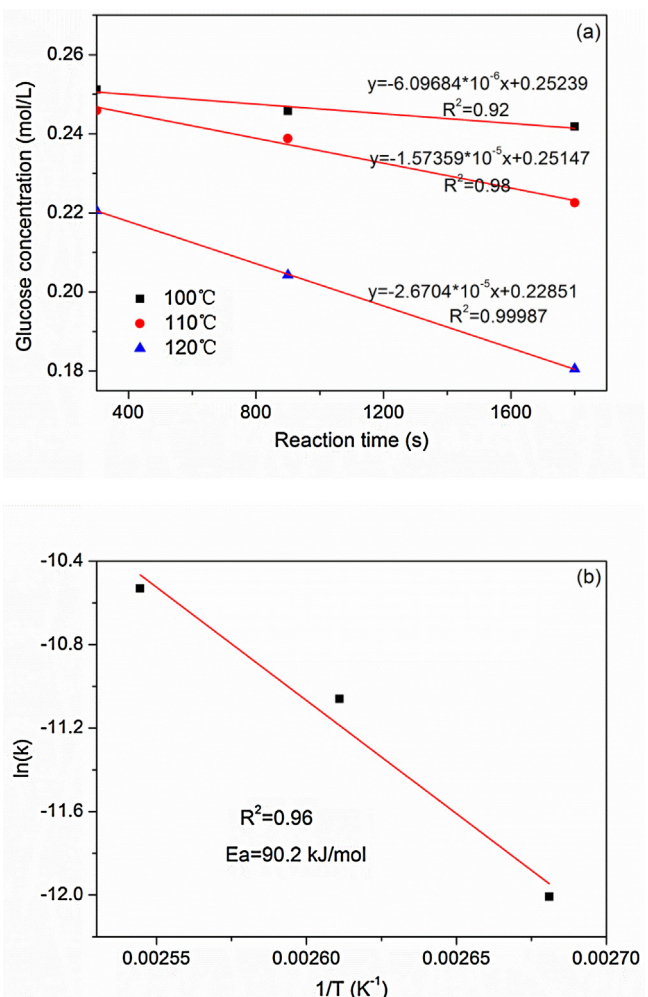


**Fig. 10.** (a) Kinetic analysis of glucose conversion in the presence of  $\text{Nb}_4\text{W}_4$  in aqueous solution. (b) Arrhenius plot.

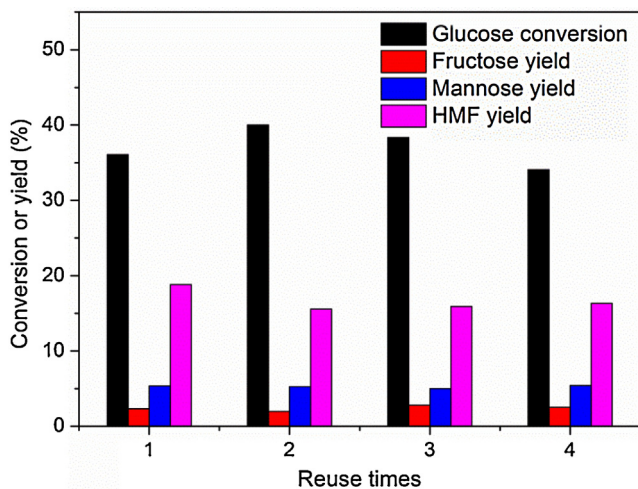


**Fig. 11.** Mesoporous  $\text{Nb}_4\text{W}_4$  oxide catalyst reusability for glucose conversion at 120 °C for 120 min.

## 4. Conclusions

In this work, we have demonstrated a facile method via evaporation-induced self-assembly to synthesize a series of ordered mesoporous bimetallic  $\text{Nb}_x\text{W}_{(8-x)}$  oxides. The characteri-

**Table 4**Catalytic behavior of  $\text{Nb}_4\text{W}_4$  and representative catalysts for the conversion of glucose in aqueous solution.

| Entry | Catalyst                                       | Time (min) | T (°C) | Conversion (%) | $\text{Y}_{\text{Fr}}\text{ (%)}$ | $\text{Y}_{\text{Man}}\text{ (%)}$ | $\text{Y}_{\text{HMF}}\text{ (%)}$ | $k\text{ (10}^{-5}\text{ s}^{-1}\text{)}$ | Ref.      |
|-------|--|------------|--------|----------------|-----------------------------------|------------------------------------|------------------------------------|---|-----------|
| 1     | $\text{AlCl}_3\text{-6H}_2\text{O}^{\text{a}}$ | 180        | 120    | 31.8           | 26.3                              | –                                  | –                                  | 4.5                                       | [13]      |
| 2     | $\text{CrCl}_3\text{-6H}_2\text{O}^{\text{a}}$ | 180        | 120    | 52.3           | 25.4                              | –                                  | –                                  | 15.8                                      | [13]      |
| 3     | Sn-Beta <sup>b</sup>                           | 180        | 120    | 67.5           | 45.3                              | –                                  | –                                  | 15.8                                      | [13]      |
| 4     | Sn-Beta <sup>b</sup>                           | 30         | 110    | 55.0           | 32.0                              | 9.0                                | –                                  | –   | [12]      |
| 5     | Sn-Beta + HCl <sup>b</sup>                     | 120        | 140    | 72.0           | 18.0                              | 2.0                                | 11.0                               | –   | [12]      |
| 6     | meso-Sn-MFI <sup>c</sup>                       | 120        | 80     | 37.0           | 27.0                              | 3.0                                | –                                  | –   | [32]      |
| 7     | $\text{Nb}_4\text{W}_4$                        | 120        | 120    | 36.1           | 2.3                               | 5.3                                | 18.8                               | 13.4                                      | This work |

<sup>a</sup> 1.0 mL  $\text{H}_2\text{O}$ , 0.25 M glucose, 25.0 mM catalyst ( $\text{AlCl}_3\text{-6H}_2\text{O}$ ,  $\text{CrCl}_3\text{-6H}_2\text{O}$ ), glucose:Sn = 200:1 (mol:mol).<sup>b</sup> 10 wt% aqueous solution of glucose, metal:glucose = 1:50 (mol:mol).<sup>c</sup> 120 mg glucose, 80 mg catalyst, 3.88 g  $\text{H}_2\text{O}$ .

zation results indicate that  $\text{Nb}_2\text{O}_5$  in  $\text{Nb}_x\text{W}_{(8-x)}$  is amorphous state while the molecular structure of  $\text{WO}_x$  over  $\text{Nb}_x\text{W}_{(8-x)}$  catalysts exists in the form of monotungstate, polytungstate and crystalline m- $\text{WO}_3$  clusters with the increasing  $\text{WO}_x$  content. The ratio of Brønsted and Lewis acidic sites can be regulated via controlling the composition of Nb and W.

$\text{Nb}_x\text{W}_{(8-x)}$  oxides are efficient catalysts for glucose conversion and  $\text{Nb}_4\text{W}_4$  is the most active one with 90.2 kJ/mol apparent activation energy. The ordered mesoporous structure and high amounts of Brønsted and Lewis acidic sites of  $\text{Nb}_4\text{W}_4$  are crucial to the excellent catalytic performance. Brønsted acid is beneficial to the formation of HMF, while Lewis acid site facilitates to yield fructose. Moreover,  $\text{Nb}_4\text{W}_4$  presents good stability upon four reaction cycles. It's envisaged that such an environmental friendly, robust and active mesoporous catalyst will hold great potential in biomass conversion.

## Acknowledgements

This work was financially supported by National Basic Research Development Program (973 Program) of China (2011CB201403), National Natural Science Foundation of China (21403269, 21273264) and Shanxi Province of China (2016021033), and Youth Innovation Promotion Association CAS (2015140).

## References

- [1] S. Zhu, J. Wang, W. Fan, *Catal. Sci. Technol.* 5 (2015) 3845–3858.
- [2] I. Delidovich, R. Palkovits, *J. Catal.* 327 (2015) 1–9.
- [3] D. Sun, Y. Yamada, S. Sato, W. Ueda, *Appl. Catal. B* 193 (2016) 75–92.
- [4] B. Mallesham, P. Sudarsanam, B.V.S. Reddy, B.M. Reddy, *Appl. Catal. B* 181 (2016) 47–57.
- [5] C.A. Antonyraj, J. Jeong, B. Kim, S. Shin, S. Kim, K.-Y. Lee, J.K. Cho, *J. Ind. Eng. Chem.* 19 (2013) 1056–1059.
- [6] S. Zhu, X. Gao, F. Dong, Y. Zhu, H. Zheng, Y. Li, *J. Catal.* 306 (2013) 155–163.
- [7] W. Deng, Q. Zhang, Y. Wang, *Sci. China Chem.* 58 (2015) 29–46.
- [8] X. Xiang, L. He, Y. Yang, B. Guo, D. Tong, C. Hu, *Catal. Lett.* 141 (2011) 735–741.
- [9] R. Bermejo-Deval, R.S. Assary, E. Nikolla, M. Moliner, Y. Román-Leshkov, S.J. Hwang, A. Palsdottir, D. Silverman, R.F. Lobo, L.A. Curtiss, M.E. Davis, *Proc. Natl. Acad. Sci. U. S. A.* 109 (2012) 9727–9732.
- [10] N. Rajabbeigi, A.I. Torres, C.M. Lew, B. Elyassi, L. Ren, Z. Wang, H.J. Cho, W. Fan, P. Daoutidis, M. Tsapatsis, *Chem. Eng. Sci.* 116 (2014) 235–242.
- [11] C. Liu, J.M. Carraher, J.L. Swedberg, C.R. Herndon, C.N. Fleitman, J.P. Tessonner, *ACS Catal.* 4 (2014) 4295–4298.
- [12] M. Moliner, Y. Roman-Leshkov, M.E. Davis, *Proc. Natl. Acad. Sci. U. S. A.* 107 (2010) 6164–6168.
- [13] J. Tang, X. Guo, L. Zhu, C. Hu, *ACS Catal.* 5 (2015) 5097–5103.
- [14] C. Loerbroks, J. van Rijn, M.P. Ruby, Q. Tong, F. Schuth, W. Thiel, *Chem. Eur. J.* 20 (2014) 12298–12309.
- [15] S. Jia, K. Liu, Z. Xu, P. Yan, W. Xu, X. Liu, Z.C. Zhang, *Catal. Today* 234 (2014) 83–90.
- [16] S.H. Mushrif, J.J. Varghese, D.G. Vlachos, *Phys. Chem. Chem. Phys.* 16 (2014) 19564–19572.
- [17] V. Choudhary, A.B. Pinar, R.F. Lobo, D.G. Vlachos, S.I. Sandler, *ChemSusChem* 6 (2013) 2369–2376.
- [18] H. Nguyen, V. Nikolakis, D.G. Vlachos, *ACS Catal.* 6 (2016) 1497–1504.
- [19] G. Lee, Y. Jeong, A. Takagaki, J.C. Jung, *J. Mol. Catal. A* 393 (2014) 289–295.
- [20] I. Delidovich, R. Palkovits, *Catal. Sci. Technol.* 4 (2014) 4322–4329.
- [21] S. Yu, E. Kim, S. Park, I.K. Song, J.C. Jung, *Catal. Commun.* 29 (2012) 63–67.
- [22] Y. Román-Leshkov, M. Moliner, J.A. Labinger, M.E. Davis, *Angew. Chem. Int. Ed.* 49 (2010) 8954–8957.
- [23] M. Moliner, *Dalton Trans.* 43 (2014) 4197–4208.
- [24] J. Dijkmans, D. Gabriels, M. Dusselier, F. de Clippel, P. Vanelderen, K. Houthoofd, A. Malfliet, Y. Pontikes, B.F. Sels, *Green Chem.* 15 (2013) 2777–2785.
- [25] R. Bermejo-Deval, R. Gounder, M.E. Davis, *ACS Catal.* 2 (2012) 2705–2713.
- [26] M. Liu, S. Jia, C. Li, A. Zhang, C. Song, X. Guo, *Chin. J. Catal.* 35 (2014) 723–732.
- [27] Y.-P. Li, M. Head-Gordon, A.T. Bell, *ACS Catal.* 4 (2014) 1537–1545.
- [28] G. Yang, E.A. Pidko, E.J.M. Hensen, *ChemSusChem* 6 (2013) 1688–1696.
- [29] S. Saravananurugan, M. Paniagua, J.A. Melero, A. Riisager, *J. Am. Chem. Soc.* 135 (2013) 5246–5249.
- [30] N. Rai, S. Caratzoulas, D.G. Vlachos, *ACS Catal.* 3 (2013) 2294–2298.
- [31] J.W. Harris, M.J. Cordon, J.R.D. Iorio, J.C. Vega-Vila, F.H. Ribeiro, R. Gounder, *J. Catal.* 335 (2016) 141–154.
- [32] P.Y. Dapsens, C. Mondelli, J. Jagielski, R. Hauert, J. Pérez-Ramírez, *Catal. Sci. Technol.* 4 (2014) 2302–2311.
- [33] L. Ren, Q. Guo, P. Kumar, M. Orazov, D. Xu, S.M. Alhassan, K.A. Mkhoyan, M.E. Davis, M. Tsapatsis, *Angew. Chem. Int. Ed.* 54 (2015) 10848–10851.
- [34] P. Carniti, A. Gervasini, F. Bossolla, V.D. Santo, *Appl. Catal. B* 193 (2016) 93–102.
- [35] J. Zhang, A. Das, R.S. Assary, L.A. Curtiss, E. Weitz, *Appl. Catal. B* 181 (2016) 874–887.
- [36] B.K. Chethana, S.H. Mushrif, *J. Catal.* 323 (2015) 158–164.
- [37] R. Bermejo-Deval, M. Orazov, R. Gounder, S.-J. Hwang, M.E. Davis, *ACS Catal.* 4 (2014) 2288–2297.
- [38] I. Delidovich, R. Palkovits, *ChemSusChem* 9 (2016) 547–561.
- [39] V. Choudhary, S.H. Mushrif, C. Ho, A. Anderko, V. Nikolakis, N.S. Marinkovic, A.I. Frenkel, S.I. Sandler, D.G. Vlachos, *J. Am. Chem. Soc.* 135 (2013) 3997–4006.
- [40] P. Wrigstedt, J. Keskkäli, M. Leskelä, T. Repo, *ChemCatChem* 7 (2015) 501–507.
- [41] I. Jiménez-Morales, M. Moreno-Recio, J. Santamaría-González, P. Maireles-Torres, A. Jiménez-López, *Appl. Catal. B* 164 (2015) 70–76.
- [42] I. Jiménez-Morales, M. Moreno-Recio, J. Santamaría-González, P. Maireles-Torres, A. Jiménez-López, *Appl. Catal. B* 154–155 (2014) 190–196.
- [43] C. Tagusagawa, A. Takagaki, A. Iguchi, K. Takanabe, J.N. Kondo, K. Ebitani, S. Hayashi, T. Tatsumi, K. Domen, *Angew. Chem. Int. Ed.* 49 (2010) 1128–1132.
- [44] C. Tagusagawa, A. Takagaki, A. Iguchi, K. Takanabe, J.N. Kondo, K. Ebitani, T. Tatsumi, K. Domen, *Chem. Mater.* 22 (2010) 3072–3078.
- [45] F. Madeira, K. Ben Tayeb, L. Pinard, H. Vezin, S. Maury, N. Cadran, *Appl. Catal. A* 443 (2012) 171–180.
- [46] E. Mena, A. Rey, S. Contreras, F.J. Beltran, *Catal. Today* 252 (2015) 100–106.
- [47] S. Zhu, X. Gao, Y. Zhu, J. Cui, H. Zheng, Y. Li, *Appl. Catal. B* 158 (2014) 391–399.
- [48] M.N. Taylor, W. Zhou, T. Garcia, B. Solsona, A.F. Carley, C.J. Kiely, S.H. Taylor, *J. Catal.* 285 (2012) 103–114.
- [49] J. Yan, G. Wu, N. Guan, L. Li, *Appl. Catal. B* 152–153 (2014) 280–288.
- [50] J. Ye, J. Liu, Z. Zou, J. Gu, T. Yu, *J. Power Sources* 195 (2010) 2633–2637.
- [51] C. Tagusagawa, A. Takagaki, A. Iguchi, K. Takanabe, J.N. Kondo, K. Ebitani, S. Hayashi, T. Tatsumi, K. Domen, *Angew. Chem. Int. Ed.* 49 (2010) 1128–1132.
- [52] S. Zhu, X. Gao, Y. Zhu, Y. Li, *J. Mol. Catal. A* 398 (2015) 391–398.
- [53] J.R. Christianson, S. Caratzoulas, D.G. Vlachos, *ACS Catal.* 5 (2015) 5256–5263.
- [54] H. Nguyen, V. Nikolakis, D.G. Vlachos, *ACS Catal.* 6 (2016) 1497–1504.
- [55] L. Petruš, M. Petrušová, Z. Hricovníková, in: A.E. Stütz (Ed.), *Glycoscience*, vol. 215, Springer, Berlin, 2001, pp. 15–41.
- [56] B.K. Chethana, D. Lee, S.H. Mushrif, *J. Mol. Catal. A* 410 (2015) 66–73.
- [57] D.W. Gardner, J. Huo, T.C. Hoff, R.L. Johnson, B.H. Shanks, J.-P. Tessonier, *ACS Catal.* 5 (2015) 4418–4422.